of the catalyst, including selectivity for the case of more complex catalytic pathways. Figure 2B suggests the local regeneration of deactivated areas as one possible starting point for such a design. In the case of island-forming reactants, for which the reaction occurs at the perimeter of these islands (*34*, *35*), the generation of additional boundaries should enhance reaction rates. What are good feedback laws for these objectives, and how can they be implemented? Hierarchical control schemes (*36*) may be key to the practical implementation of real-time feedback with finely distributed actuation.

References and Notes

1. J. A. Lundqvist *et al.*, *Proc. Natl. Acad. Sci. U.S.A.* **95**, 10356 (1998).
2. Y. S. Matros, G. A. Bunimovich, *Catal. Rev.-Sci. Eng.* **38**, 1 (1996).
3. M. X. Yang, D. H. Gracias, P. W. Jacobs, G. A. Somorjai, *Langmuir* **14**, 1458 (1998).
4. K. Wong, S. Johansson, B. Kasemo, *Faraday Discuss.*, **105**, 237 (1996).
5. R. Srinivasan *et al.*, *AIChE J.* **43**, 3059 (1997).
6. A. L. Lin *et al.*, *Phys. Rev. Lett.* **84**, 4240 (2000).
7. V. Petrov, V. Gaspar, J. Masere, K. Showalter, *Nature* **361**, 240 (1993).
8. M. Kim *et al.*, *Science* **292**, 1357 (2001).
9. H. H. Rotermund, *Surf. Sci. Rep.* **29**, 265 (1997).
10. _____, W. Engel, M. Kordesch, G. Ertl, *Nature* **343**, 355 (1990).
11. S. Jakubith, H. H. Rotermund, W. Engel, A. v. Oertzen, G. Ertl, *Phys. Rev. Lett.* **65**, 3013 (1990).
12. F. Mertens, R. Imbihl, *Nature* **370**, 124 (1994).
13. M. D. Graham *et al.*, *Science* **264**, 80 (1994).
14. J. Lauterbach *et al.*, *Physica D* **123**, 493 (1998).
15. S. Y. Shvartsman, E. Schütz, R. Imbihl, I. G. Kevrekidis, *Phys. Rev. Lett.* **83**, 2857 (1999).
16. M. Kolodziejczyk, R. E. R. Colen, B. Delmon, J. H. Block, *Appl. Surf. Sci.* **121**, 480 (1997).
17. F. Esch *et al.*, *Catal. Lett.* **52**, 85 (1998).
18. Y. S. Matros, *Can. J. Chem. Eng.* **74**, 566 (1996).
19. J. G. Khinast, D. Luss, *Comput. Chem. Eng.* **24**, 139 (2000).
20. S. Kádár, J. Wang, K. Showalter, *Nature* **391**, 770 (1998).
21. O. Steinbock, V. Zykov, S. C. Müller, *Nature* **366**, 322 (1993).
22. E. D. Sontag, *Mathematical Control Theory: Deterministic Finite-Dimensional Systems* (Springer-Verlag, Berlin, ed. 2, 1998).
23. E. Ott, C. Grebogi, J. A. Yorke, *Phys. Rev. Lett.* **64**, 1196 (1990).
24. V. S. Zykov, A. S. Mikhailov, S. C. Müller, *Phys. Rev. Lett.* **78**, 3398 (1997).
25. D. Semowogerere, M. F. Schatz, *Bull. Am. Phys. Soc.* **45**, 46 (2000).
26. R. Roy, K. S. Thornburg Jr., *Phys. Rev. Lett.* **72**, 2009 (1994).
27. V. K. Vanag, L. Yang, M. Dolnik, A. M. Zhabotinsky, I. R. Epstein, *Nature* **406**, 389 (2000).
28. Desired spatiotemporal heating patterns could be programmed into the control computer by using LabVIEW. In addition, it was possible to control the laser spot on the surface by hand directly, using the computer mouse. This joystick mode establishes—as in computer games or flight simulators—a direct feedback with the human brain as image processor and control action calculator. For our computer-controlled feedback experiments, real-time image processing and desired rules for the heating patterns and intensities were implemented in software.
29. O. Steinbock, J. Schütze, S. C. Müller, *Phys. Rev. Lett.* **68**, 248 (1992).
30. A. P. Munuzuri, M. Dolnik, A. M. Zhabotinsky, I. R. Epstein, *J. Am. Chem. Soc.* **121**, 8065 (1999).
31. In our experiments, the Pt(110) single-crystal sample was kept in an ultrahigh-vacuum apparatus. The surface was prepared by Ar-ion sputtering and annealing to about 1100 K. The quality of the surface preparation was checked with low-energy electron diffraction.
32. H. H. Rotermund, G. Haas, R. U. Franz, R. M. Tromp, G. Ertl, *Science* **270**, 608 (1995).
33. We have measured the spatiotemporal temperature profile of our laser spot using a cooled infrared (IR) camera with a temperature resolution of 0.05 K at room temperature. From those IR images we deduced a maximum differential temperature rise at the spot of about 15 K; typically, we worked at powers giving a temperature rise of 2 to 3 K over an area of ~80 μm in diameter. Detailed heat balance simulations, including radiation and conduction, showed that only 5 ms were needed to locally establish this differential temperature rise, confirming our experimental observation of a heat quench in less than 20 ms. In other words, the temperature rises and returns to its background state essentially instantaneously with the movement of the laser spot.
34. S. Völkening, J. Wintterlin, *J. Chem. Phys.* **114**, 6382 (2001).
35. D. Y. Kuan, H. T. Davis, R. Aris, *Chem. Eng. Sci.* **38**, 719 (1983).
36. G. J. Pappas, G. Lafferriere, S. Sastry, *IEEE Trans. Autom. Control* **45**, 1144 (2000).
37. M. D. Graham *et al.*, *Phys. Rev. E* **52**, 76 (1995).

38. We gratefully acknowledge partial support by the Office of Naval Research (I.G.K. and H.H.R.), NSF, Air Force Office of Scientific Research, and the Humboldt Foundation (I.G.K.), and by a Marie Curie Fellowship (A.G.P.) under contract HPMFCT-2000-00685. We thank M. Pollmann for the measurement of Fig. 1C and S. Shvartsman for many discussions.

19 June 2001; accepted 28 August 2001

Submicrometer Metallic Barcodes

Sheila R. Nicewarner-Peña,[1] R. Griffith Freeman,[2] Brian D. Reiss,[1] Lin He,[2] David J. Peña,[1] Ian D. Walton,[2] Remy Cromer,[2] Christine D. Keating,[1]* Michael J. Natan[2]*

We synthesized multimetal microrods intrinsically encoded with submicrometer stripes. Complex striping patterns are readily prepared by sequential electrochemical deposition of metal ions into templates with uniformly sized pores. The differential reflectivity of adjacent stripes enables identification of the striping patterns by conventional light microscopy. This readout mechanism does not interfere with the use of fluorescence for detection of analytes bound to particles by affinity capture, as demonstrated by DNA and protein bioassays.

Multiplexing and miniaturization are becoming pervasive themes in bioanalysis. The push to measure ever-increasing numbers of species from smaller and smaller sample volumes has led to innovative devices for sample manipulation [e.g., chip-based microfluidics (*1*)] and ingenious approaches to simultaneous measurement capabilities (e.g., mi-

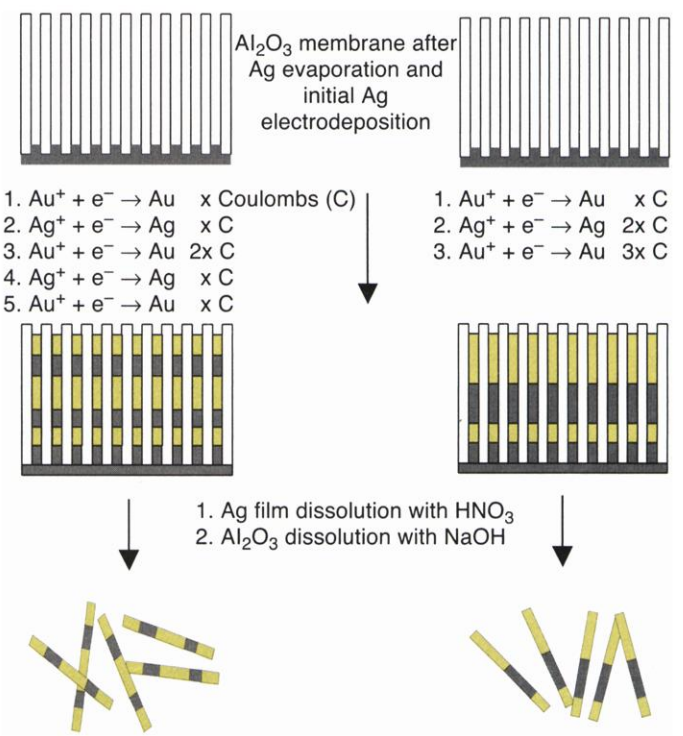

Fig. 1. Synthesis of barcoded particles.

croarrays and encoded, micrometer-sized polymeric beads). Microarrays (*2*) exploit positional encoding to carry out large numbers of analyses in parallel, but they can suffer from slow diffusion of analytes to the surface (*3*) and limitations in the range of analyte concentrations that may be detected simultaneously. In the case of microbeads, encoding is accomplished by incorporation of molecules (*4*–*6*) or, as recently described, nanoparticles (*7*) with distinctive fluorescent signatures. Arrays of beads in solution circumvent the shortcomings of planar microarrays for assay development.

However, the number of bead-based assays that can be performed simultaneously is limited by the number of spectrally distinguishable fluorophores. This number is further constrained when, as is often the case, a fluorophore is required for analyte quantitation. If encoding did not depend on fluorophore incorporation, then particles should retain the advantages of solution arrays with increased levels of multiplexing. Here, we describe the electrochemical manufacture and optical characterization of striped, cylindrically shaped metal nanoparticles that can be identified by the pattern of differential optical reflectivity of adjacent stripes. Because many thousands of uniquely identifiable particles can be prepared, and because such particles can be used in fluorescence– and mass spectrometry–based assays, they enable a wide variety of bioanalytical measurements.

Suspensions of barcoded particles were prepared by sequential electrochemical reduction of metal ions into the pores of membrane templates (*8, 9*), followed by particle release (Fig. 1) (*10*). A silver film deposited on the backside of an Al_2O_3 membrane serves as the working electrode for reduction of metal ions from solution. The structure of each particle type is controlled by (i) the membrane pore diameter, which sets the particle width; (ii) the sequence of metal ions introduced into solution, which defines the number and pattern of metal stripes; and (iii) the charge passed in each step, which dictates stripe length. Alumina or polycarbonate membrane templates with nominal pore diameters ranging from 15 nm to 12 μm are commercially available (*11*); well-defined alternative templates potentially include those generated by interference photolithography (*12*), self-organization of block copolymers (*13*), and electrochemical oxidation of nanoindented bulk Al (*14*). To date, we have incorporated seven different metals (Pt, Pd, Ni, Co, Ag, Cu, and Au) in segments as short as 10 nm and as long as several micrometers, and have prepared particles with as many as 13 distinguishable stripes. Moreover, the process used to fabricate these materials is amenable to automation. Particle characterization has included techniques well suited to metal nanoparticles [electron and scanning probe microscopies, optical extinction spectra (*15*)] as well as those typically applied to bulk materials [atomic absorption, optical reflectivity (*16*)].

Images of a 4.5-μm-long Au cylinder with a single Ag segment near one end were generated by electron and optical microscopy (Fig. 2A). Although the electron micrograph has higher resolution, the striping pattern is clearly apparent in the optical image. The physical basis for the optical contrast be-

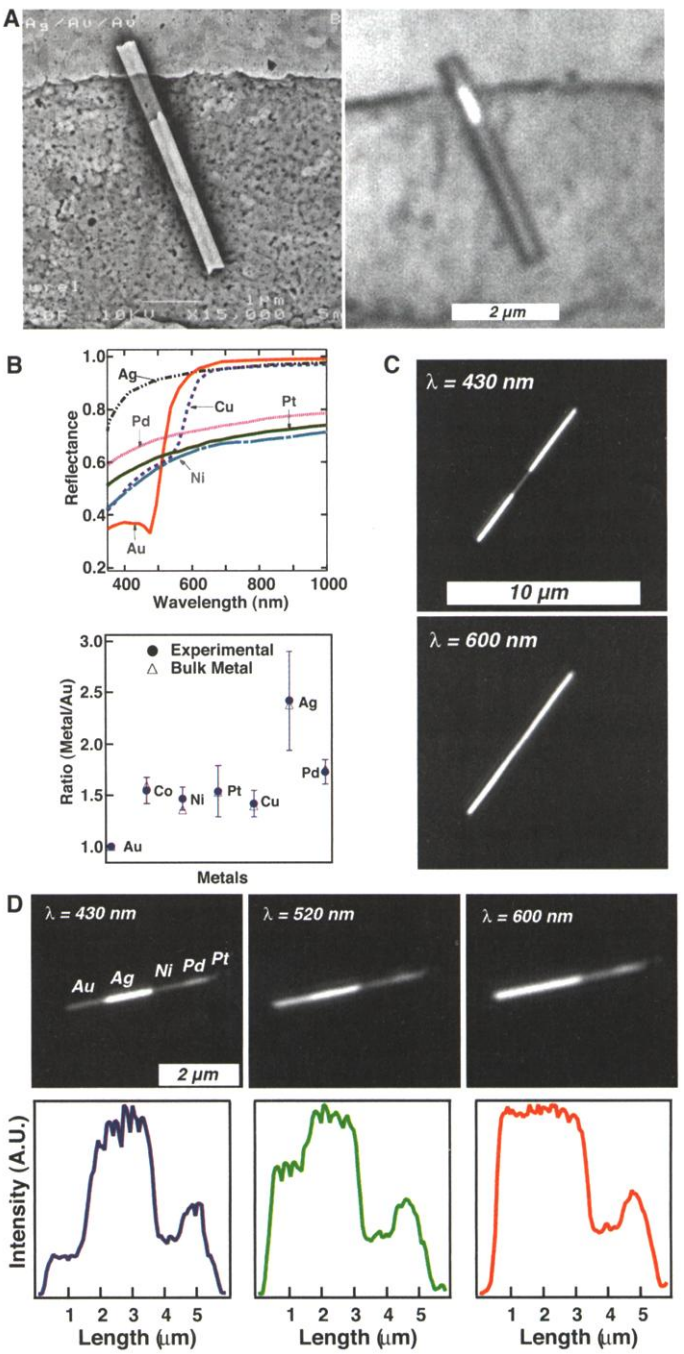

Fig. 2. Optical properties of cylindrical striped particles. **(A)** FE-SEM image (left) and optical microscope image (right) of the same Au-Ag-Au particle. Contrast in the FE-SEM image results from differences in backscattered electron intensity from the two metals. [A reflective Au background is used in (A) but not in the other optical images here.] **(B)** Upper panel: Wavelength dependence of reflectivity for bulk metals [this graph was generated from values reported in (*17*)]. Lower panel: Ratio of reflected intensities for various metals versus Au at 430 nm for bulk materials (open triangles) and for striped particles. For the latter, values were experimentally determined using reflectance optical microscopy. **(C)** Reflectance optical microscopy image of an Ag-Au-Ag barcode rod (length ~10 μm). Top: High contrast was observed between Ag (brighter sections) and Au (dark middle section) with 430-nm illumination. Bottom: No contrast using 600-nm excitation. **(D)** Reflectance optical microscopy images and line profiles for a particle of composition Au-Ag-Ni-Pd-Pt with illumination at 430 nm, 520 nm, and 600 nm, respectively. Samples were mounted on glass slides and imaged with a Nikon TE-300 inverted microscope equipped with a bright-field reflectance filter set (containing a 50/50 beam splitter) using a 100× oil immersion lens (NA = 1.3). A 100-W Hg lamp with a 430-, 520-, or 600-nm (±10 nm) bandpass filter was used for excitation, as indicated. All particles shown here and in subsequent figures were prepared by electrodeposition in the pores of 0.2-μm (*11*) Anodisc (Whatman) alumina membranes (*8*–*10*).

[1]Department of Chemistry, Pennsylvania State University, 152 Davey Laboratory, University Park, PA 16802, USA. [2]SurroMed Inc., 2375 Garcia Avenue, Mountain View, CA 94043, USA.

*To whom correspondence should be addressed. E-mail: keating@chem.psu.edu, mnatan@surromed.com

tween Au and Ag segments is the difference in reflectivity of the two metals. Reflectance data for bulk metals (*17*) are plotted in Fig. 2B (top panel) as a function of incident wavelength. Although barcoded particles have at least one dimension on the order of the incident wavelength, their reflectivity properties are largely bulk-like. For example, Fig. 2B indicates that bulk Ag is ~2.5 times as reflective as bulk Au at 430 nm, whereas at 600 nm they are equivalent; we observe this experimentally in the striped particles. Figure 2C shows an Au-Ag-Au particle imaged at these two wavelengths. The brighter sections correspond to Ag (and are ~2.5 times as bright); the darker section corresponds to Au. Illuminating the same particle with 600-nm light yields an image in which the metal segments are indistinguishable.

We have compared the experimentally observed values for Au, Ag, and several other metals to those expected for bulk materials. These data (Fig. 2B, lower panel) indicate that agreement between metal stripes and their bulk counterparts is quite good. At 430-nm excitation, the greatest contrast observed is that between Au and Ag. However, several other metals have intermediate reflectivities, suggesting the possibility of using more than two intensity levels for optical encoding. Images of a single multimetal particle with blue, green, and red illumination are shown in Fig. 2D; the wavelength dependence of reflectivity for each segment follows that predicted in Fig. 2B. Note that Au is readily distinguished from Ni, Pt, or Pd by its high reflectivity at 600 nm. The linescans below each image of Fig. 2D show variations in intensity of reflected light along the length of the particles. At 520 nm, four different metals (Au, Ag, Ni, and Pd) could be differentiated on the basis of the intensity of their reflectivities in the linescan.

Optical reflectivity can be used to read out the striping pattern encoded in the metal particles during their synthesis. Most of the metal segments shown in Fig. 2 were relatively large, but much shorter segments can be synthesized. The lower limit for stripe length will arise not in preparation, but rather in identification of the striping patterns. Given that a preferred mode of readout is by optical microscopy, the diffraction-limited coding potential of barcode rods can be estimated as follows. At the Rayleigh limit, the smallest distance between two resolvable points is = $\lambda/2(NA)$, where NA is the numerical aperture of the objective lens (*18*). Thus, optical resolution is optimized when particles are read using short wavelengths and high NA (e.g., NA = 1.4, an oil-immersion lens). This gives $400/(2 \times 1.4) = 143$ nm minimal spacing between segments. For reliable readout of the barcode patterns, stripe lengths should be well above the optical resolution limit. For example, for a 6.5-μm coding length with 500-nm stripes (well above the diffraction-limited spacing), a total of 13 segments are obtained. With two metals (e.g., Au and Ag), the number of barcodes possible is 4160 (*19, 20*). This value is already far greater than the number of distinguishable fluorophore-based tags of any variety (*6, 7, 21, 22*). With three metals, 8.0×10^5 distinctive striping patterns are possible (*23*).

For adjacent metals with high contrast, it should be possible to optically detect very short stripes. To that end, we have synthesized and optically detected Ag segments as small as 50 nm in Au rods. Figure 3 shows optical and field-emission scanning electron microscopy (FE-SEM) images of the same Au-Ag multistriped particle, which contains Ag stripes of lengths from 240 nm down to 60 nm, separated by 550-nm Au segments. Because the Ag stripes are separated by several hundred nm, they are optically detectable. Thus, it should be possible to distinguish large numbers of barcode patterns.

Polydispersity in the length of electroplated segments is a critical factor in determining how many distinguishable particle "flavors" can be prepared. For Au cylinders, an 8% standard deviation in overall length has been reported (*10*). The monodispersity of striped particle synthesis can be seen in Fig. 4A, an optical reflectivity image for a batch of Au-Ag-Au-Ag particles. The overall length of

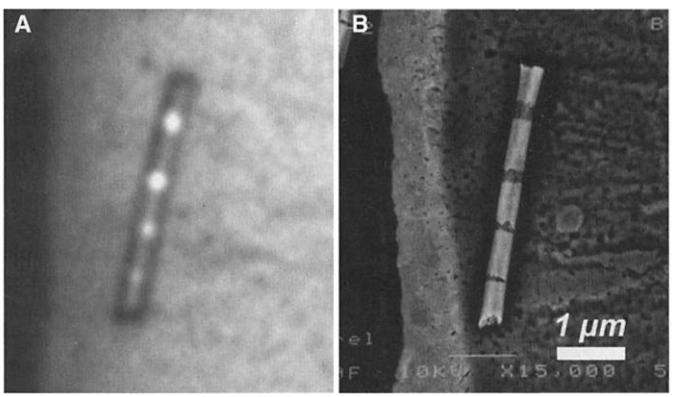

Fig. 3. Optical (**A**) and FE-SEM (**B**) images of an Au-Ag multistripe particle with ~550-nm Au stripes and Ag stripes of 240, 170, 110, and 60 nm (top to bottom). The same particle is shown in both images. Particles were placed on an Au finder grid (Electron Microscopy Sciences) to facilitate identification and imaging of the same particles by both techniques. FE-SEM data were acquired using backscattering detection on a JEOL JSM-6320F at Accurel Inc. (Sunnyvale, California).

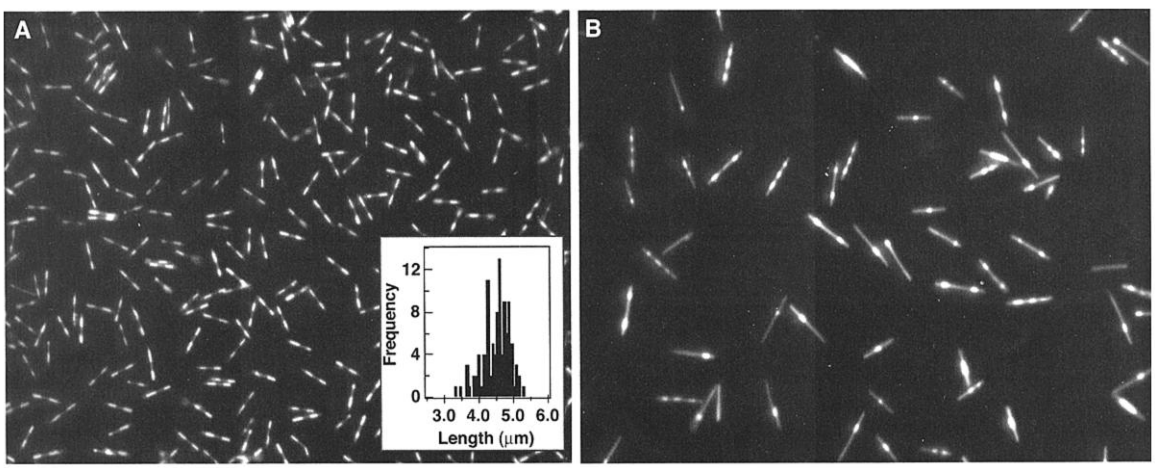

Fig. 4. Optical images of barcoded particles. (**A**) A population of particles of "flavor" 0110011, where 0 denotes Au and 1 denotes Ag segments. The inset shows a histogram of particle lengths for 106 particles in this image. Particle length was 4.5 ± 0.4 μm, or a ±9% variation in overall particle length. Images were acquired with a Zeiss Axiovert 100 microscope with a Plan APO 100× 1.4 NA objective. Illumination was provided by 175-W Xe lamp and LiquidLight Guide (Sutter Instruments, Novato, California) filtered with a HQ 405-nm, 20-nm bandpass filter (Chroma Inc., Brattleboro, Vermont). Illumination was split with a 50/50 BS (Chroma). (**B**) Mixture of nine barcode batches with different striping patterns. Particle "flavors" in increasing binary order: 0000000, 0000001, 0000010, 0000100, 0001000, 0001010, 0011100, 0100010, and 0101010.

these particles, as determined by optical microscopy, is 4.5 ± 0.4 μm. With 10% standard deviation in stripe length, it should be possible to distinguish between one and two adjacent stripes, down to stripe lengths of ≤350 nm (*24, 25*). Figure 4B shows a mixed population of ~4.3-μm-long particles with several different barcode patterns, each of which is readily identifiable. The particle striping pattern can be used to encode information, for example, the identity of surface capture chemistry for a particle-based bioassay.

Derivatization chemistries for metal surfaces and metal nanoparticles are well developed, ranging from nonspecific direct adsorption (e.g., of polymers or proteins) to more specific metal-adsorbate interactions such as occur in alkanethiol self-assembled monolayers (*26*). This rich chemistry enables the coupling of a wide variety of capture reagents onto barcoded particles. In particular, monolayers that resist nonspecific binding by proteins have been described (*27*). The striping pattern can be used to identify which chemistry has been immobilized on the particle, in much the same way as position encodes information in conventional microarray experiments. Although the particles are micrometers in length, their relatively small width makes it possible to keep the particles in suspension by agitation to provide more rapid mixing between the particles and target molecules.

Perhaps the most straightforward means to detect and/or quantify analyte binding to barcoded particles is by fluorescence imaging. Because analyte identity is determined by barcode reflectivity readout, only one fluorophore is necessary to detect a variety of biomolecules. If multiple fluorophores are used, an even greater level of multiplexing is possible (e.g., with n barcode patterns and three fluorophores, $3n$ different assays could be done simultaneously). To demonstrate that barcoded rods can be used as supports for bioassays, we have adapted DNA hybridization and immunoassays for use on barcodes. Figure 5A shows a particle-based "sandwich" hybridization assay. A 24-nucleotide oligomer (the analyte) binds to a 12-nucleotide capture sequence on the particle surface and is later detected by addition of a 12-nucleotide probe sequence that is complementary to the remaining 12 nucleotides and carries a 3′ fluorescent tag (*28*). Each individual particle can be seen in both the fluorescence (Fig. 5A, i) and reflectivity (ii) images. When the analyte is omitted, a very low fluorescence background is observed (iii), and particles are visible only in the reflectivity image (iv). The selective detection of DNA hybridization on single optically encoded particles is an important first step toward multiplexed hybridization assays.

We have also performed simultaneous sandwich immunoassays on two different barcoded particles (**1** = 4-μm-long Au-Ag-Au, **2** = 8-μm-long Au-Ni-Au). Rods of type **1** were derivatized with capture antibody to human immunoglobulin G (IgG), whereas rods of type **2** were similarly derivatized with capture antibody to rabbit IgG. The samples were mixed and exposed to both analytes (i.e., human IgG and rabbit IgG), after which they were exposed to secondary antibodies. To test the selectivity of the chemistries, we labeled each secondary antibody with fluorophores of different colors (green for antibody to human IgG, red for antibody to rabbit IgG). The results of this experiment are shown in Fig. 5B; a reflectance image enables the identification of the particles, and the fluorescence images show the same particles with filter sets for green and red fluorescence, respectively. Note that the green fluorescence emanates predominantly from particles of type **1**, and red predominantly from type **2**. This indicates that the specific capture chemistries on the two classes of particles were able to selectively bind their target analytes.

Although a very low level of nonspecific binding can be observed (i.e., as a small amount of red fluorescence on the Ag-Au-Ag particles, and green on the Au-Ni-Au particles), these results demonstrate that simultaneous immunoassays can be performed on rods and that the reflectivity image is sufficient for identification of the capture chemistry on a given particle. Thus, even if we had used only one fluorophore in this experiment, it would have been possible to distinguish between the human and rabbit IgG solely on the basis of the barcode pattern of the particles.

To a certain extent, the barcode pattern is visible in the fluorescence images. This can be explained to a first approximation simply by the wavelength-dependent reflectivities of

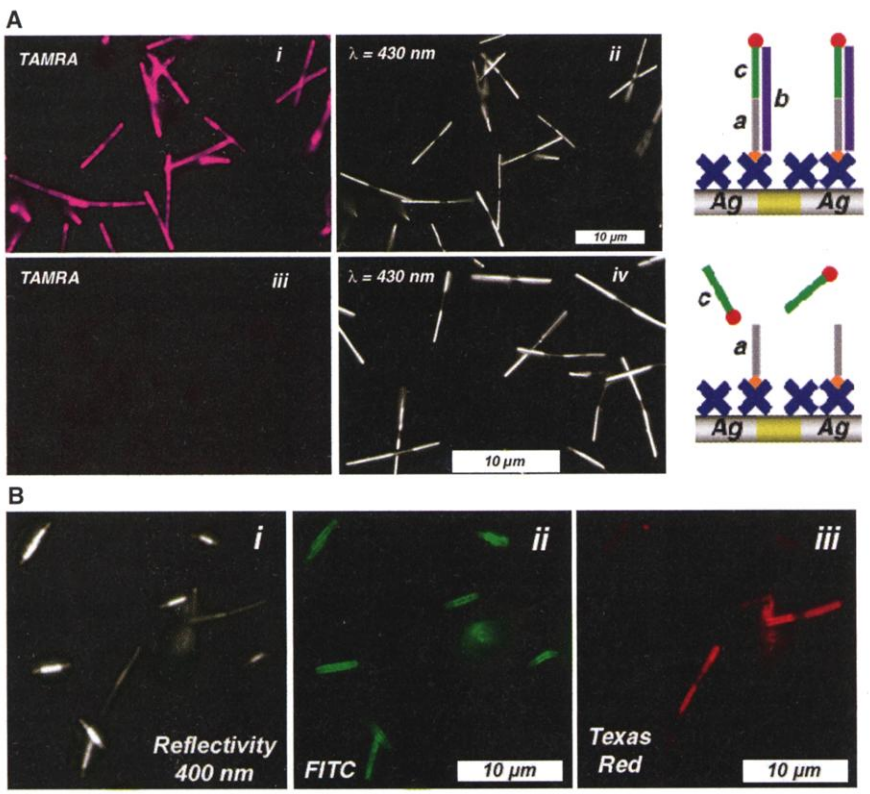

Fig. 5. Bioassays performed on barcoded particles using fluorescence detection. (**A**) "Sandwich" DNA hybridization assay [see scheme on right (*29*)]. Panel (i) reveals the fluorescence readout; (ii) shows the rod ID. The analyte, **b**, was omitted in the control sample. Panels (iii) and (iv) show the fluorescence readout and the rod ID, respectively. Fluorescence images were obtained using the "wide green" filter cube (Nikon). (**B**) A simultaneous sandwich immunoassay performed on barcode rods. A scheme depicting the configuration of such assays is shown below the microscopy images (*30*). Panel (i) shows the reflectance optical microscopy image, which gives the barcode rod ID; (ii) and (iii) show the fluorescence readout with FITC and Texas Red filter sets, respectively. All three images are of the same sample location. Samples for (A) and (B) were mounted between a glass cover slip and slide using a Secure-Seal spacer (Molecular Probes, Eugene, Oregon) and viewed with optical and instrumentation as in Fig. 2.

these metals. By choice of metal and fluorophore, it is also possible to "hide" the barcode pattern in fluorescence images.

As interest grows in carrying out comprehensive analyses on classes of biologically relevant molecules (e.g., genomics, proteomics, metabolomics), there is a demand for very high-level multiplexing in small sample volumes, and thus a corresponding need for new readout mechanisms. Solution arrays of highly encodable and chemically diverse nanoparticles, such as those described herein, offer an intriguing solution to both requirements.

References and Notes

1. D. J. Harrison *et al.*, *Science* **261**, 895 (1993).
2. V. G. Cheung *et al.*, *Nature Genet. Suppl.* **21**, 15 (1999).
3. M. R. Henry, P. Wilkins Stevens, J. Sun, D. M. Kelso, *Anal. Biochem.* **276**, 204 (1999).
4. S. A. Dunbar, J. W. Jacobson, *Clin. Chem.* **46**, 1498 (2000).
5. D. R. Walt, *Science* **287**, 451 (2000).
6. B. J. Battersby *et al.*, *J. Am. Chem. Soc.* **122**, 2138 (2000).
7. M. Han, X. Gao, J. Z. Su, S. Nie, *Nature Biotechnol.* **19**, 631 (2001).
8. D. Almalawi, C. Z. Liu, M. Moskovits, *J. Mater. Res.* **9**, 1014 (1994).
9. J. C. Hulteen, C. R. Martin, *J. Mater. Chem.* **7**, 1075 (1997).
10. B. R. Martin *et al.*, *Adv. Mater.* **11**, 1021 (1999).
11. The membranes used in this work are Al_2O_3 and have a nominal pore diameter of 200 nm. However, the pores are 200 nm only at the surface of the membrane. SEM measurements indicate that the pores widen to ~400 nm in the central region of the membrane, with an average diameter of 318 ± 50 nm. All of the particles discussed in this report have diameters in this range [as determined by transmission electron microscopy (TEM) and SEM].
12. T. A. Savas, M. L. Schattenburg, J. M. Carter, H. I. Smith, *J. Vac. Sci. Technol. B* **14**, 4167 (1996).
13. T. Thurn-Albrecht *et al.*, *Science* **290**, 2126 (2000).
14. H. Masuda *et al.*, *Adv. Mater.* **13**, 189 (2001).
15. K. C. Grabar *et al.*, *Anal. Chem.* **69**, 471 (1997).
16. Particles were characterized electrochemically during the deposition process. After preparation, they were characterized by the following techniques: TEM, SEM, FE-SEM, energy-dispersive x-ray scattering, macroscopic extinction, microscopic reflectivity, atomic absorption, and chemical treatment (e.g., selective dissolution of less noble segments).
17. D. R. Lide, *CRC Handbook of Chemistry and Physics* (CRC Press, Cleveland, OH, ed. 71, 1990), pp. 12-87–12-102.
18. S. Inoue, K. R. Spring, *Video Microscopy* (Plenum, New York, ed. 2, 1997).
19. The equation for calculation of unique sequences for a barcode of n metals and s stripes is n^s for particles read in only one direction (i.e., having "start" markers), and $[n^s + n^{\mathrm{ceil}(s/2)}]/2$ for particles read randomly in either direction (*20*). Thus, for a 6.5-μm particle comprising 500-nm stripes of two different metals, use of a 500-nm "start" marker gives $2^{12} = 4096$, whereas a 13-segment particle with no "start" marker gives $(2^{13} + 2^7)/2 = 4160$.
20. The formula for the case with two different metals is described in N. Hoffman, *2-Year Coll. Math. J.* **9**, 267 (1978). For the more general case, see www.research.att.com/~njas/sequences/transforms2.html.
21. M. Bruchez Jr., M. Moronne, P. Gin, S. Weiss, A. P. Alivisatos, *Science* **281**, 2013 (1998).
22. W. C. W. Chan, S. Nie, *Science* **281**, 2016 (1998).
23. In practice, the striping pattern can be combined with different particle lengths and stripe compositions to yield either a greater total number of distinctive patterns or, perhaps more important, a set of particles selected for ease of identification (i.e., by computer software).
24. More than 95% of all 1× segments will be shorter than 500 nm + 2(10%) = 600 nm, and >95% of all 2× segments will be longer than 1000 nm − 2(10%) = 800 nm (*25*). For 350-nm segments, >95% of all 1× segments will be <420 nm, whereas 95% of all 2× segments will be >560 nm. Although the differences in these two lengths cannot be directly measured by optical microscopy, they should be distinguishable by differences in intensity. Note that we have prepared 230-nm stripes with 16% standard deviation, and we routinely prepare particles in the 4- to 8-μm range with <10% standard deviations in total length.
25. D. A. Skoog, D. M. West, F. J. Holler, *Fundamentals of Analytical Chemistry* (Saunders, New York, ed. 6, 1992), p. 42.
26. A. Ulman, *An Introduction to Ultrathin Films from Langmuir-Blodgett to Self-Assembly* (Academic Press, New York, 1991).
27. P. Harder, M. Grunze, G. M. Whitesides, P. E. Laibinis, *J. Phys. Chem. B* **102**, 426 (1998).
28. DNA sequences: (a) "capture" oligonucleotide: 5′-biotin-AAAAAACGCATTCAGGAT-3′, (b) analyte: 5′-TACGAGTTGAGAATCCTGAATGCG-3′, (c) "detection" oligonucleotide: 5′-TCTCAACTCGTA-fluor-3′, where fluor = tetramethylrhodamine (TAMRA).
29. Particles were first derivatized with NeutrAvidin (0.1 mg/ml, Pierce) by adsorption of the protein to the surface for 1 hour in 0.3 M phosphate-buffered saline (PBS, pH 7.0). This was followed by attachment of a biotinylated capture 12-nucleotide oligomer, **a**. The sample was prehybridized with a solution of 0.1% SDS in 0.3 M PBS for 15 min. The analyte, **b**, a 24-nucleotide oligomer (4 μM) was hybridized with **a** for 2 hours by heating to 60°C with passive cooling to room temperature in the water bath. The samples were rinsed and detection proceeded by hybridization with a TAMRA-labeled detection oligomer, **c** (4 μM), for 2 hours at 30°C. After hybridization, the samples were rinsed first with 1% SDS in 0.3 M PBS, then with 0.1% SDS in 0.3 M PBS, and finally with 0.3 M PBS.
30. Particles were derivatized with 16-mercaptohexadecanoic acid to which the capture antibody, **a**, was covalently attached using standard carbodiimide chemistry. For this assay, Au-Ag-Au rods were derivatized with antibody to human IgG (Fc specific), and Au-Ni-Au rods were derivatized with antibody to rabbit IgG (Fc specific). After attachment of the capture antibody, the rods were further derivatized with poly(ethylene glycol) (PEG) using a 1% solution of *bis*-aminated PEG. Nonspecific sites on the capture antibody were blocked using a 1% solution of bovine serum albumin (BSA) in 0.3 M PBS (pH 7.0). The analytes, **b**, in this case human IgG and rabbit IgG, were mixed together to a final concentration of 0.05 mg/ml, added to a mixture of derivatized barcoded rods, and allowed to incubate for 30 min. After incubation, the sample was rinsed several times in 0.3 M PBS (pH 7.0) buffer and then incubated for an additional 30 min with a mixture of the detection antibodies, **c** [antibody to rabbit IgG (heavy and light chains) labeled with Texas Red; antibody to human IgG (γ specific) labeled with fluorescein isothiocyanate (FITC)]. After incubation with **c**, the sample was rinsed several times in buffer.

31. We thank T. Carado, P. Smith, W. Stonas, K. Shale, S. Norton, and L. Dietz for their help with particle synthesis and optical characterization. Supported by NIH grant HG02228 (C.D.K.).

30 May 2001; accepted 14 August 2001

Deposition of Conformal Copper and Nickel Films from Supercritical Carbon Dioxide

Jason M. Blackburn, David P. Long, Albertina Cabañas, James J. Watkins*

Device-quality copper and nickel films were deposited onto planar and etched silicon substrates by the reduction of soluble organometallic compounds with hydrogen in a supercritical carbon dioxide solution. Exceptional step coverage on complex surfaces and complete filling of high-aspect-ratio features of less than 100 nanometers width were achieved. Nickel was deposited at 60°C by the reduction of bis(cyclopentadienyl)nickel and copper was deposited from either copper(I) or copper(II) compounds onto the native oxide of silicon or metal nitrides with seed layers at temperatures up to 200°C and directly on each surface at temperatures above 250°C. The latter approach provides a single-step means for achieving high-aspect-ratio feature fill necessary for copper interconnect structures in future generations of integrated circuits.

The increasing complexity and decreasing dimensions of devices for microelectronic, system-on-a-chip, data storage, and other applications are placing stringent demands on deposition technologies that, to date, have not been fully satisfied. These include reductions in the thermal budget during fabrication, mitigation of the negative environmental impact of current processes, conformal coverage of complex surfaces, and complete filling of narrow, high-aspect-ratio structures (*1*). The difficulties associated with achieving the latter two requirements are particularly severe. For example, to keep pace with the historical increase in processor speed popularly referred to as Moore's Law, Cu interconnect structures for integrated circuits must drop below 100 nm in width with aspect ratios that exceed 3 after 2005. According to the Semiconductor Industry Association's International Technology Roadmap for Semiconductors

Department of Chemical Engineering, University of Massachusetts, Amherst, MA 01003, USA.

*To whom correspondence should be addressed. E-mail: watkins@ecs.umass.edu